DOI: 10.1002/anie.201202481

Biosensors

Optimized Use of Reversible Binding for Fast and Selective NMR Localization of Caged Xenon**

*Martin Kunth, Jörg Döpfert, Christopher Witte, Federica Rossella, and Leif Schröder**

Xenon-129 is an extremely sensitive NMR probe, as illustrated by its large chemical shift range in many different molecular environments.[1] The noble gas can be spin-hyperpolarized (hp) to achieve a 10^4-fold increase in NMR signal and in solution it can reversibly bind to host structures (for example, cryptophanes), inducing a large change in resonance frequency.[2] These properties have motivated the design of xenon biosensors[3] with the biologically compatible gas acting as a functionalized contrast agent for "molecular imaging". Improved detection techniques are crucial to realize the potential of xenon biosensors. It was recently speculated[4] that chemical exchange saturation transfer (CEST) could improve detection of xenon biosensors, as it is mainly limited by the signal-to-noise ratio (SNR) of the Xe@solution peak. Herein, NMR localization of caged xenon is demonstrated by free dissolved xenon with single-shot echo-planar imaging (EPI) and optimized use of reversible binding by CEST. This yields several significant improvements, including subsecond detection of caged xenon, magnetic resonance imaging (MRI) with xenon host concentrations in the nanomolar range, high spectral selectivity, and time-resolved studies of cryptophane diffusion.

Xenon-based sensors have been developed to detect the presence of a certain analyte[4,5] or reveal various biochemical binding events,[3,6–8] including transferrin-mediated uptake.[9] They often rely on small changes in chemical shift (typically $\delta \approx 1$ ppm) to determine if they are bound to their target and to differentiate between different sensors; thus any detection method should conserve high spectral selectivity. As the amount of caged ^{129}Xe is expected to be small, direct detection requires extensive signal averaging, especially for MRI.[10] Exploiting the reversible binding of xenon to its host has been suggested as a way to utilize all available hyperpolarized atoms in solution. Two such methods have been developed: direct detection by repetitive cage-selective excitation[11] and indirect detection using Hyper-CEST.[12] These initial implementations suffer from limited spatial resolution and spectral selectivity. Selective excitation is strongly limited by the cage and ^{129}Xe concentration in several aspects. First, it requires relatively high cage concentrations (200–300 μM)[4,11] as it uses conventional signal averaging, with SNR increasing only with the square root of the number of acquisitions. Second, to increase cage occupancy, high ^{129}Xe concentrations (ca. 4.5 mM in solution at 1 atm Xe)[4] are often applied. This necessitates batch mode production to obtain high purity hyperpolarized Xe. Third, when using slice selection, the magnetic field gradient broadens the cage resonance and the method loses spectral selectivity.[11] The Hyper-CEST approach on the other hand preserves slice selection and has been demonstrated with lower Xe concentrations (ca. 200 μM). It utilizes the reversible binding in a more efficient way, by encoding the Xe@cage signal in the Xe@solution peak. As it is a differencing technique, it requires a minimum of two acquisitions (reference and on-resonant saturation) with comparable starting conditions, which necessitates reliable delivery of Xe into solution. Previous implementations of Hyper-CEST have been hampered by long acquisition times with multiple Xe re-deliveries over several minutes per image.[12] This made the method sensitive to instabilities in Xe delivery into solution and limits further encoding of the spectral dimension of different sensors.[13]

Herein, we demonstrate that ^{129}Xe concentrations as low as about 100 μM are sufficient to perform single-shot MRI. This allows Xe to be used directly from the polarizer in continuous flow without purification, thus improving reproducibility of delivery of hp Xe. Re-delivery can now be reduced to its absolute minimum; that is, one dissolution per CEST image. With batch-mode production and single filling of the NMR tube with Xe gas, CEST would not be possible owing to signal loss from repetitive excitation and relaxation.

To demonstrate the detection limits of this technique, we performed measurements at physiological temperature (310 K) to accelerate the chemical exchange and increase Hyper-CEST efficiency. Hp Xe was bubbled into a phantom (Supporting Information, Figure S1) containing 250 nM solution of cryptophane-A monoacid cages (CrA-ma, Figure 1a; a precursor for biosensor synthesis) in 95% H_2O/5% DMSO. The CrA-ma was imaged using an EPI sequence (Supporting Information, Figure S2) with a CEST saturation pulse of $B_1 =$ 19 μT for 26 s (total imaging time including gas deliveries ca. 102 s). The CEST data show excellent response (Figure 1c) with clear localization of CrA-ma in the image (Figure 1d). Under these conditions, [Xe@solution] is about 361 μM (ca. 95 μM ^{129}Xe) and circa 45% occupancy of cages, the concentration of NMR-active cages is only 30 nM (see the Supporting

[*] M. Kunth,[+] J. Döpfert,[+] Dr. C. Witte, F. Rossella, Dr. L. Schröder
ERC Project BiosensorImaging
Leibniz-Institut für Molekulare Pharmakologie (FMP)
13125 Berlin (Germany)
E-mail: lschroeder@fmp-berlin.de
Homepage: http://www.fmp-berlin.de/schroeder/

[+] These authors contributed equally to this work.

[**] This work has been supported by the European Research Council under the European Community's Seventh Framework Programme (FP7/2007-2013)/ERC grant agreement no. 242710 and the Human Frontier Science Program. The authors would like to thank Stefan Klippel for fruitful discussions regarding the dialysis tubing.

Supporting information for this article is available on the WWW under http://dx.doi.org/10.1002/anie.201202481.

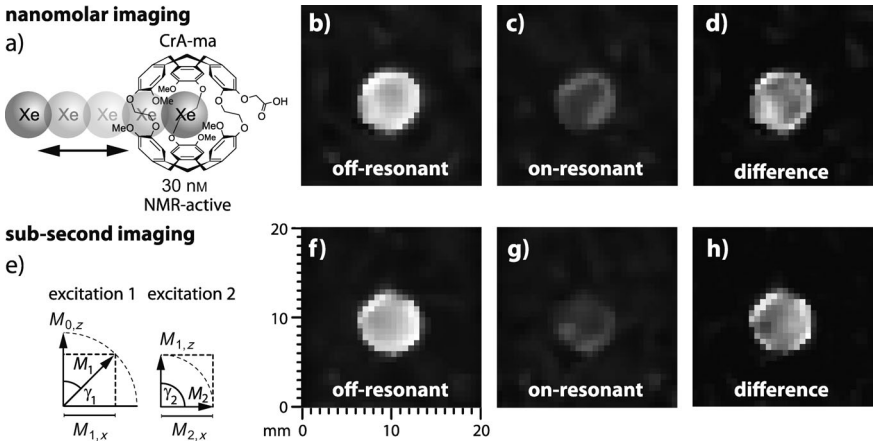

Figure 1. Detection limits of Hyper-CEST EPI acquired at $T = 310$ K. a) CrA-ma for fast reversible binding of hyperpolarized Xe. b–d) ^{129}Xe CEST imaging of the distribution of the cage molecules at a total concentration of 250 nM and an NMR-active fraction of 30 nM. The images were acquired employing a cw-saturation pulse (length $t_{sat} = 26$ s, amplitude $B_1 = 19$ μT), once off-resonant (b) ($SNR_b \approx 5$) and once on-resonant (c) ($SNR_c \approx 3$) with Xe@CrA-ma. Prior to each scan, fresh hp ^{129}Xe was bubbled into solution for 25 s. d) Difference image illustrating localization of the caged ^{129}Xe ($SNR_{CEST,d} \approx 2$). e)–h) Subsecond imaging of 50 μM CrA-ma with single delivery of hp ^{129}Xe ($SNR_f/SNR_g/SNR_{CEST,h} \approx 6/2/2$). e) CEST data of the solution was collected with shared magnetization after single hyperpolarization (smashCEST; see also the Supporting Information) using a variable flip angle excitation. With a saturation pulse length of $t_{sat} = 450$ ms ($B_1 = 19$ μT) and an EPI scan time of 19.8 ms per image, the total acquisition time adds up to only 940 ms. Although the post-processed images are shown, all SNR specifications refer to the raw ^{129}Xe images.

Information). This significantly improves on the fastest approach so far, selective excitation with [Xe@solution] of about 4500 μM, circa 96% occupancy, circa 83 μM NMR-active cages and comparable spatial resolution in 15 s.[4] Using selective excitation for nM cage detection would require multiple re-deliveries of Xe, with acquisition times of well over 100 s. The circa 2750-fold decrease in concentration compared to Reference [4] does not require 2750^2-fold increase in acquisition time when making optimized use of the chemical exchange through Hyper-CEST.

A second experiment was performed to explore minimum acquisition times; subsecond MRI after a single delivery of hp ^{129}Xe ([CrA-ma] = 50 μM, Xe gas fraction = 5%). To acquire two measurements, we combined Hyper-CEST EPI with a variable flip angle[14] (Figure 1e; Supporting Information, Figure S4). A first saturation pulse is applied off-resonant prior to excitation with a 45° flip angle (Figure 1f), and the second saturates CrA-ma on-resonant before exciting the residual longitudinal magnetization with a 90° flip angle (Figure 1g). Figure 1h shows the difference image for CEST pulses of 450 ms and $B_1 = 19$ μT. The total acquisition time for the two scans was about 940 ms. This demonstrates snap-shot NMR localization of caged Xe at fairly low concentrations (8.9 μM NMR-active cage; [^{129}Xe@solution] ca. 238 μM). This sensitivity improvement allows new imaging applications, such as acquisition of full z-spectra images, that is, sweeping the saturation frequency to encode the chemical shift dimension. To demonstrate chemical selectivity, we developed a model system to tune the Xe@cage chemical shift. This is achieved by varying the DMSO/water ratio of the solvent (Supporting Information, Figure S6). To simulate multiplexing of differently functionalized cages, we used a two compartment phantom (Supporting Information, Figure S1) and tuned the Xe@cage peak in the different compartments to be about 131 Hz ($\delta = 1.2$ ppm) apart (Figure 2a). This was achieved by using 10% vol. DMSO in the outer and 20% vol. DMSO in the inner compartment. Data were acquired with a saturation pulse of $B_1 = 1$ μT, $t_{sat} = 4$ s and steps of 20 Hz in saturation frequency taking images every 33 s after Xe re-delivery. Figure 2b shows the z-spectrum calculated from area-normalized signal intensities of different regions of interest (ROIs), and Figure 2c,d show ^{1}H and ^{129}Xe reference images. The method clearly separates the two different solutions with CEST response in one compartment while the other remains untouched (Figure 2e,f).

False-color encoding of the separate responses (Figure 2g) illustrates good sensitivity with unprecedented high chemical specificity while still performing slice selection (selective readout of resonances separated by about 235 Hz was demonstrated in Reference [4], but without the ability to perform slice selection). Only the red area shows some blue contributions, which is possibly due to bleeding of the broader left saturation dip into the right dip. The CEST profile for the higher DMSO content shows a broader response and a stronger absolute signal decrease (Supporting Information, Figure S7). This solution has a higher concentration of Xe (ca. 25–30% according to the baselines in Figure 2b), which might increase the cage occupancy if the binding constant is not reduced significantly by the higher DMSO concentration. In any case, the CEST effect seems to benefit from faster exchange, as represented by the increased dip width.

As another application of fast MRI of caged Xe we performed time-resolved studies of CrA-ma diffusion through dialysis tubing. Such tubing with MWCO = 10 kDa containing 500 μM cage in DMSO was placed inside the phantom at $t =$ 0 min to provide a strong concentration gradient. Outside the tubing was DMSO, initially with no CrA-ma. Xe was bubbled into both volumes. Figure 3a shows a series of images (acquired every 33 s) with an increasing CEST response in the outer compartment. The signal from this area shows an exponential decay (Figure 3b). Further analysis reveals good agreement with a monoexponential increase in CEST response (time constant $\tau = 53$ min). This could be accelerated to $\tau = 17$ min or 4 min by piercing the membrane 2 or 3 times with a 350 μm needle (Figure 3c). False-color encoding of the increasing CEST response from CrA-ma diffusion to the outer compartment is depicted in Figure 3d (for animated versions, see the Supporting Information, Figure S8). The CEST approach detects quite low cage concentrations (15 μM) in the outer compartment, as confirmed by

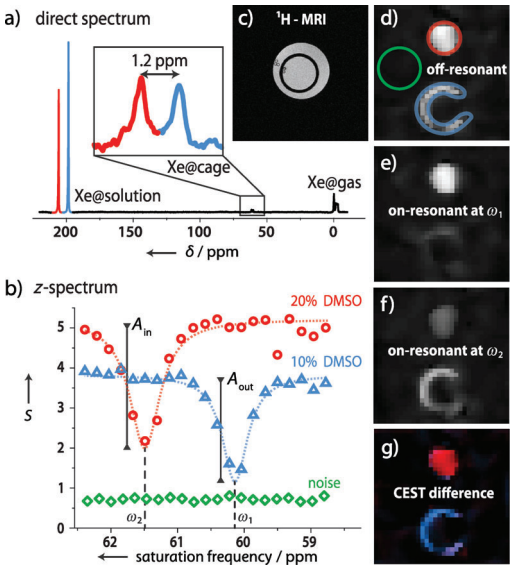

Figure 2. Chemically selective ^{129}Xe NMR imaging at $T = 293$ K. a) Direct ^{129}Xe NMR spectrum (16 averages) of a 10 μM cage dissolved in water with different DMSO fractions in the inner (20%) and the outer compartment (10%) of the bubbling phantom (see ^{1}H MRI (c)), leading to a chemical shift separation for both the Xe@cage and the Xe@solution peaks. The Xe@cage resonances are separated by $\omega_2 - \omega_1 = 1.2$ ppm (131 Hz at 9.4 T). The *z* spectrum with 20 Hz ($\delta = 0.18$ ppm) increments of the saturation frequency depicted in (b) illustrates the high selectivity and sensitivity of the CEST response. The data points result from averaging the signal over the ROIs shown in the off-resonant CEST image (d) for each saturation frequency. The amplitudes of the CEST response $A_{in} = 3.2$ and $A_{out} = 2.7$ are obtained from Lorentzian fits (dashed lines). Subtraction of the two on-resonant images (e) and (f) from the off-resonant image (d) yields the color-encoded CEST difference image (g), which allows for a clear spatial discrimination of the two Xe@cage resonances ($SNR_{CEST,red}/SNR_{CEST,blue} \approx 3/2$ refer to the raw ^{129}Xe images). The displacement between the inner and the outer compartment in (d)–(g) is a chemical shift artefact that originates from the frequency separation of the Xe@solution peaks (805 Hz; ca. 17 pixel shift).

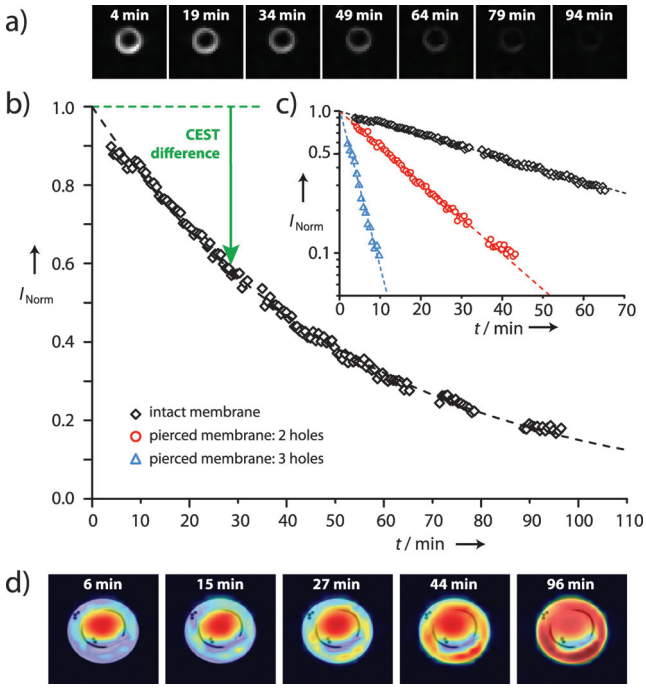

Figure 3. Visualization of CrA-ma diffusion at $T = 295$ K through dialysis tubing with Hyper-CEST EPI. At $t = 0$, CrA-ma is only present in the inner compartment (500 μM concentration). a) ^{129}Xe Hyper-CEST EPI images with presaturation at the Xe@cage frequency ($t_{sat} = 7$ s, $B_1 = 12$ μT) at different times *t* illustrates the gradual decay of the signal in the outer compartment owing to diffusion of cage molecules through the intact membrane ($SNR_{image1} \approx 16.7$). b) The time-dependent mean signal of a ROI in the outer compartment shows an exponential decay. The dashed green line represents the extrapolated off-resonant signal intensity; the length of the green arrow corresponds to the CEST difference which increases in time. Missing data points in the plot are due to acquisitions of high-resolution multislice proton images to monitor the position of the membrane. c) Signal decays show good agreement with monoexponential behavior (dashed lines) for the intact membrane (black diamonds) and intentionally pierced membranes with two (red circles) and three (blue triangles) 350 μm holes. The obtained decay constants of $\tau_{intact} = 53$ min, $\tau_{2\ holes} = 17$ min, and $\tau_{3\ holes} = 4$ min, respectively, indicate faster diffusion through damaged membranes. d) Visualization of the increase in cage concentration in the outer compartment for the intact membrane by overlaying a ^{1}H-MR image with CEST difference images. (A movie of the diffusion process for all three complete datasets can be found in the Supporting Information, Figure S8.)

UV spectrometry (see the Supporting Information). Cage occupancy at the given Xe concentration (ca. 2.40 mM) should not exceed 93% (based on $K_M = 6000\,L\,mol^{-1}$), as K_M in DMSO is expected to be lower than in water. Therefore, the concentration of NMR-active cages is ≤ 3.6 μM at $t = 4$ min and changes in the CEST response can be seen quite soon. This experiment demonstrates the feasibility of time resolved biosensor uptake studies for future in vivo applications. Such a model experiment would be extremely difficult with selective excitation owing to replacing the pure Xe atmosphere after a few images of which each would require too much time compared to the diffusion time scale.

This technique is also applicable with other fast encoding schemes, for example, balanced steady-state free precession, which may be better suited to in vivo or in vitro applications, as EPI will be affected by a reduced T_2*.

In conclusion, we demonstrated that optimized use of reversible Xe binding to a host allows significant improvement for ^{129}Xe NMR imaging. It allows efficient NMR detection even if the fraction of caged Xe is $< 2\%$ and is in the range of 10^{-8} M. In fact, efficient contrast can be easily achieved once the Xe concentration threshold for single-shot imaging is surpassed. Although the fraction of occupied cages decreases with reduced concentration of Xe@solution, the amplification through CEST can compensate for this allowing for snap-shot MRI of caged Xe while preserving high chemical selectivity. This technique could find various applications in future biosensor applications in vivo and in vitro.

Experimental Section

NMR experiments were performed on a 9.4 T NMR spectrometer (Bruker Biospin, Ettlingen, Germany) with gradient coils for imaging and a variable temperature unit. A 10 mm inner-diameter double-resonant probe (^{129}Xe and ^{1}H), was used for excitation and detection.

The gas flow was controlled by flow controllers at the sample gas outlet. Hyperpolarized ^{129}Xe was generated by spin exchange optical pumping (ca. 16% polarization) in a custom-designed continuous-flow setup using a gas mixture of 2% Xe (26.4% natural abundance of ^{129}Xe), 10% N_2, and 88% He (5%/10%/85% for the smashCEST experiment). The gas mix was directly bubbled into solution after polarization (Supporting Information, Figure S1). When not mentioned otherwise, for each image the samples were bubbled for 20 s at a total flow rate of 0.07 SLM followed by an 8 s delay (to allow bubbles to collapse) before signal acquisition. ^{129}Xe Hyper-CEST EPI images were acquired with a slice-selective 90°gaussian shaped excitation pulse, 20×20 mm^2 field of view, 32×32 matrix size, Fourier acceleration factor of 1.68 resulting in 19 phase encoding lines, double sampling, 20 mm slice thickness, echo time = 5.7 ms, and an acquisition time of 19.8 ms (Supporting Information, Figure S2). All images were acquired with 625 μm in plane resolution and processed using an adaptive weights smoothing filter with a local quadratic model. SNR determination of the ^{129}Xe raw images is given in the Supporting Information.

Received: March 30, 2012
Published online: July 13, 2012

Keywords: biosensors · imaging agents · magnetic resonance imaging · NMR spectroscopy · xenon

[1] B. M. Goodson, *J. Magn. Reson.* **2002**, *155*, 157 – 216.
[2] T. Brotin, J. P. Dutasta, *Chem. Rev.* **2009**, *109*, 88 – 130.
[3] M. M. Spence, S. M. Rubin, I. E. Dimitrov, E. J. Ruiz, D. E. Wemmer, A. Pines, S. Q. Yao, F. Tian, P. G. Schultz, *Proc. Natl. Acad. Sci. USA* **2001**, *98*, 10654 – 10657.
[4] N. Kotera, N. Tassali, E. Léonce, C. Boutin, P. Berthault, T. Brotin, J. P. Dutasta, L. Delacour, T. Traoré, D. A. Buisson, F. Taran, S. Coudert, B. Rousseau, *Angew. Chem.* **2012**, *124*, 4176 – 4179; *Angew. Chem. Int. Ed.* **2012**, *51*, 4100 – 4103.
[5] J. M. Chambers, P. A. Hill, J. A. Aaron, Z. Han, D. W. Christianson, N. N. Kuzma, I. J. Dmochowski, *J. Am. Chem. Soc.* **2009**, *131*, 563 – 569.
[6] Q. Wei, G. K. Seward, P. A. Hill, B. Patton, I. E. Dimitrov, N. N. Kuzma, I. J. Dmochowski, *J. Am. Chem. Soc.* **2006**, *128*, 13274 – 13283.
[7] V. Roy, T. Brotin, J. P. Dutasta, M. H. Charles, T. Delair, F. Mallet, G. Huber, H. Desvaux, Y. Boulard, P. Berthault, *ChemPhysChem* **2007**, *8*, 2082 – 2085.
[8] A. Schlundt, W. Kilian, M. Beyermann, J. Sticht, S. Günther, S. Höpner, K. Falk, O. Roetzschke, L. Mitschang, C. Freund, *Angew. Chem.* **2009**, *121*, 4206 – 4209; *Angew. Chem. Int. Ed.* **2009**, *48*, 4142 – 4145.
[9] C. Boutin, A. Stopin, F. Lenda, T. Brotin, J. P. Dutasta, N. Jamin, A. Sanson, Y. Boulard, F. Leteurtre, G. Huber, A. Bogaert-Buchmann, N. Tassali, H. Desvaux, M. Carriere, P. Berthault, *Bioorg. Med. Chem.* **2011**, *19*, 4135 – 4143.
[10] C. Hilty, T. J. Lowery, D. E. Wemmer, A. Pines, *Angew. Chem.* **2006**, *118*, 76 – 79; *Angew. Chem. Int. Ed.* **2006**, *45*, 70 – 73.
[11] P. Berthault, A. Bogaer *t*Buchmann, H. Desvaux, G. Huber, Y. Boulard, *J. Am. Chem. Soc.* **2008**, 130, 16456 – 16457.
[12] L. Schröder, T. J. Lowery, C. Hilty, D. E. Wemmer, A. Pines, *Science* **2006**, *314*, 446 – 449.
[13] T. Meldrum, L. Schröder, P. Denger, D. E. Wemmer, A. Pines, *J. Magn. Reson.* **2010**, *205*, 242 – 246.
[14] L. Zhao, R. Mulkern, C. H. Tseng, D. Williamson, S. Patz, R. Kraft, R. L. Walsworth, F. A. Jolesz, M. S. Albert, *J. Magn. Reson. Ser. B* **1996**, *113*, 179 – 183.

